Application of Laser Diagnostics to a Green Manufacturing Project

James B. Martlew, William R. DeKam
Claudia M. Fajardo (project advisor)
Western Michigan University, Kalamazoo, MI 49008-5343
Email: james.b.martlew@wmich.edu

Abstract

Industrial paint curing ovens are commonly used in the manufacture of consumer products. Many of these ovens rely on hot air jets to supply the energy necessary to cure paint coatings. Paint curing is an energy intensive process, and a large percentage of the energy supplied to curing ovens is lost through the open entrance and exit doors. The inability to effectively contain the hot air within the oven significantly increases energy consumption and manufacturing costs of the painted product. As part of a large-scale effort aimed at reducing energy consumption in industrial paint curing ovens, a full-scale, computational fluid dynamics (CFD) model is being developed to capture the energy transport within the oven and to the surroundings. Since the hot air jets are crucial to oven operation, their characteristics must be accurately modeled. To address this need, this senior capstone project focused on designing and constructing a scaled, bench-top model of an industrial oven, incorporating a round and a planar jet. Using advanced laser diagnostics, two-dimensional mean velocities and turbulence intensity fields, as well as velocity profiles were measured at various downstream locations from the nozzle exit.

1. Introduction

Industrial ovens are used across many industries and can be found in applications such as curing, drying, annealing, and baking. They generally take the form of a long, open-ended corridor, which can be heated electrically or by burning a fuel such as natural gas. Product is generally conveyed through the open ends on a continuous basis, sitting on a belt system or hanging from an overhead track. When natural gas is used for convective heating, energy is often delivered in the form of hot air directed through overhead nozzles positioned near the walls on either side of the product flow. These hot air jets impinge on the floor surface and spread out before buoyantly rising again. This motion spreads the energy of the heated air more evenly, theoretically producing a uniform vertical temperature distribution.

Industrial surface curing, in particular, is the process by which polymer-coated parts are heated until the polymer chains cross-link, causing the surface to harden. The necessary high temperature exposure times required to achieve curing means that this process can be energy intensive and costly. As a result of the common, open-ended design, a percentage of the energy supplied for the curing process is lost with the heated air escaping through the entrance and exit doors. This problem is compounded by the effects of cooler ambient air, which then flows into the oven to replace the hot air lost.

This process, schematically illustrated in Figure 1a, has undesirable consequences. First, more fuel or electricity must be used to make up for this loss and maintain minimum required oven temperatures, which translates into higher costs. As a side effect, heat escaping from the oven

raises the environment temperature, making conditions uncomfortable for plant workers in the summer months. Secondly, the non-uniform temperature gradient that develops through the interior affects productivity and part quality. The influx of cold air at either end generates temperature gradients from floor to ceiling and from the interior outward. Thus, a part conveyed through for curing experiences a range of temperatures across its surface that varies depending on its position in the oven. As a result, the coating across the part cures at different rates, and the production line must be slowed down sufficiently to assure that specified curing occurs on surfaces exposed to lower temperatures, reducing part throughput.

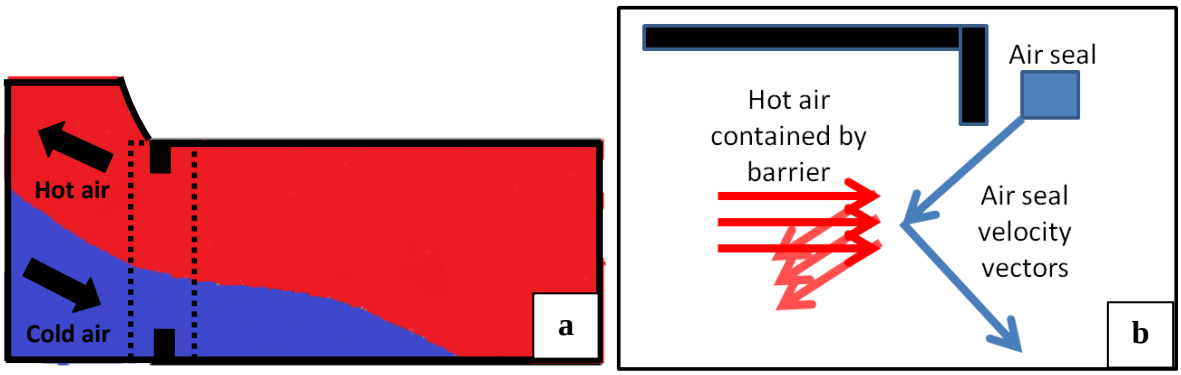

Figure 1: Cross sectional view of an oven exit as heat escapes and cold air infiltrates (a); as well as an illustration of air seal operation (b).

This problem may be at least partially circumvented by the use of air seals (or air curtains). An air seal utilizes long, thin nozzles to blow a fast moving sheet of air across the opening, separating internal and external air masses and redirecting the buoyant, hot air back into the oven (Figure 1b). In many cases, the primary (stock) air seals do not provide a sufficient barrier, which has led to the addition of secondary air seal systems in order to mitigate the heat loss problem. These secondary systems are typically installed on an ad-hoc basis, without prior analysis of optimal placement and geometry. Further improvements in energy containment can be realized with a more refined configuration. However, a detailed study of thermal transport in the oven is needed to characterize the interactions between the hot internal air mass and various air seal placement options.

As part of a large scale effort to reduce energy consumption in industrial ovens, an ongoing graduate project focuses on modeling the aforementioned oven using Ansys Fluent software. The model reproduces oven geometry and operating conditions to simulate air motion and heat transfer both throughout the oven interior and at the openings to the surrounding air. The intent is to develop a reliable representation of the oven and simulate the effect of varied air seal configurations on mitigating energy losses, in order to identify promising design options for implementation.

a. Problem Definition and Objectives

While a geometrically accurate model of the large-scale oven has been developed using Ansys Fluent (Figure 2), boundary conditions at the exit of interior air jet nozzles, which supply the hot air for the curing process, are unknown. This precludes accurate simulation of thermal transport in the large-scale oven and hence optimization of the air seal system. The goal of this project is

to overcome this difficulty by measuring relevant boundary conditions required by the large-scale model. Specifically, the objective is to quantify the turbulence intensity present in the air jet at the nozzle exit and downstream.

In addition to serving as boundary conditions for the large-scale model, these experimentally measured quantities provide significant insight into the dynamics of jets produced with different geometry nozzles.

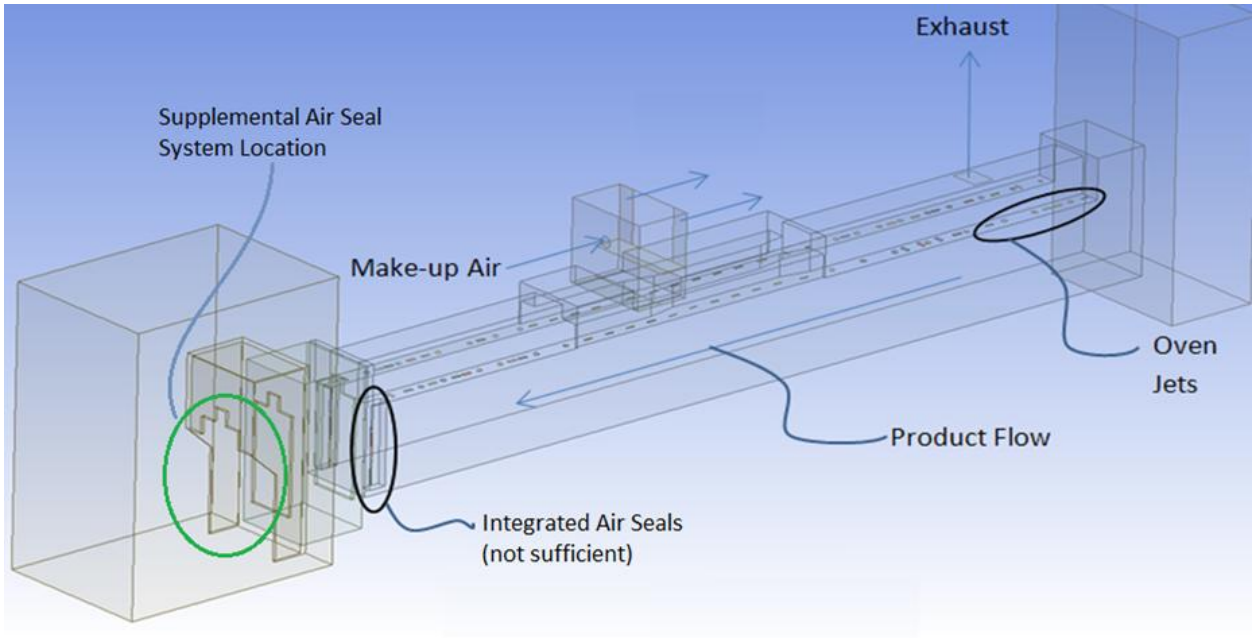

Figure 2: Geometry and features of the large-scale industrial oven modeled using Ansys Fluent.

2. Experimental Approach

Due to the difficulty of making comprehensive measurements in the large-scale oven, a scaled replica of an oven section was designed and constructed to support laboratory experiments. To scale the model, the Reynolds number (*Re*) (Eq. 1) at the nozzle exit and the ratio of the height above the oven floor to the nozzle diameter (*h/D*) were maintained constant. In the case of the rectangular nozzle, the hydraulic diameter (D_H) (Eq. 2) was used in all calculations. The exit mean velocity was measured on-site for a range of rectangular and conical nozzles, in the large scale oven, operated without the burner. Using an average Reynolds number of 45,000 calculated from these measurements, as well as the *h/D* value of 16.7, a target nozzle exit velocity of 18 m/s was selected for the scaled model, which corresponds to 10 m/s in the actual, large-scale oven. Additional parameters are shown in Table. 1.

$$\mathrm{Re} = \frac{\rho V D}{\mu} = \frac{V D}{\nu} \qquad \textbf{Eq. 1}$$

$$D_H = \frac{4A}{P} \qquad \textbf{Eq. 2}$$

	Lab Model			
Reynolds Number	Velocity at Nozzle Exit (m/s)	Conical Nozzle Diameter (mm)	Rectangular Nozzle Length (mm)	Rectangular Nozzle Width (mm)
48,500	18	41	152	47.6

Table 1: Experimental parameters for bench-top laboratory model.

The two-component velocity fields, from which turbulence intensity were computed, were measured using planar particle image velocimetry (PIV). PIV is a non-intrusive laser diagnostic technique that relies on the Mie scattering of tracer particles seeded into the flow [1]. The tracer particles are illuminated by two closely spaced laser pulses and the scattered light is recorded on digital media. The resulting pairs of images are then cross-correlated to calculate the most probable particle displacement, from which the two-component velocity fields are calculated.

a. Experimental Setup and Equipment

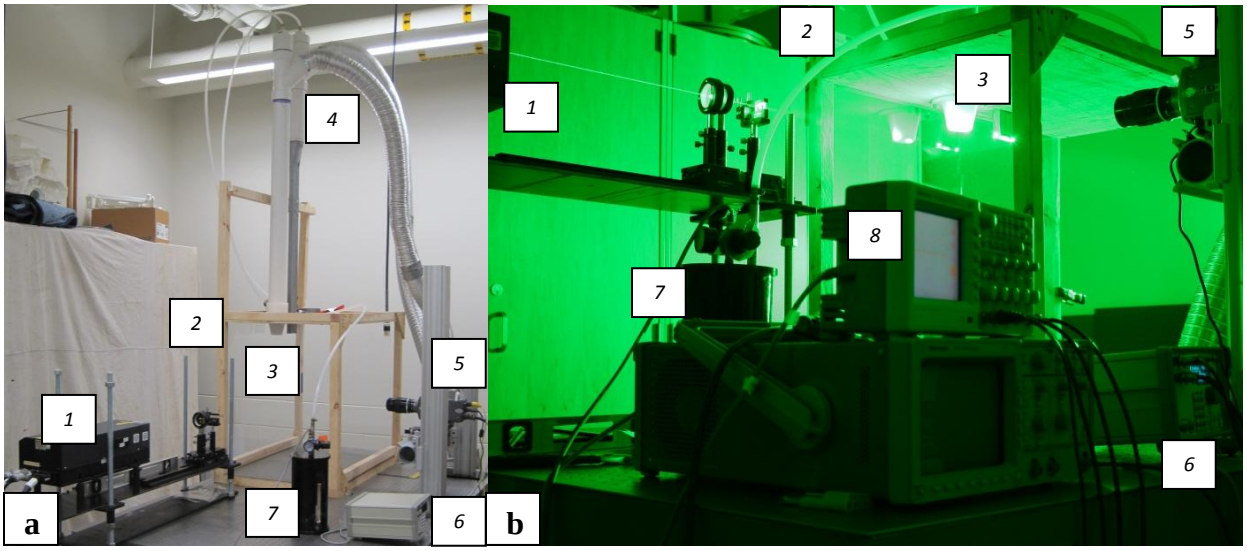

Figure 3: (a) Complete test setup showing the laser and optics (1), wooden frame (2), conical and rectangular nozzles (3), nozzle feed tubes with air and seeding supply connections (4), high speed camera (5), pulse generator (6) and seeding generator (7). (b) Close up view of the setup operating with the oscilloscope in the foreground (8) and the nozzles illuminated by the diverging laser light sheet.

The physical bench-top model, designed and built in house, consisted of a wooden frame 36 inches long, 20.75 inches wide and 28.5 inches high using oriented strand board (OSB) for floor and ceiling panels (Figure 3a,b: 2). The OSB floor panel was further covered with a piece of 18-gauge sheet metal to create a flat, smooth impingement surface. The nozzles were positioned 3.7 inches off the clear Plexiglas back wall and 4.6 inches apart (Figure 3a,b: 3). Because the actual distance between adjacent jets varies in the full scale oven, the spacing in the laboratory setup was based on the average value.

The conical nozzle was machined from a 6-inch diameter cylinder of polyethylene stock and was connected to a 3-inch inner diameter, 3.2 foot long PVC pipe to feed the nozzle with fully developed turbulent flow. The planar nozzle was constructed of sheet metal to create an exit with the desired 2.71 inch x 0.923 inch rectangular cross section. The tube was 2.8 feet long to generate the desired fully developed flow. The lengths (L) needed to produce this flow were calculated according to Eq. 3 [2], where D represents the inner diameter of the tube (or hydraulic diameter of the rectangular tube, D_H). A PVC-wye was installed at the inlet of each tube to mix the air with the seeding particles (Figure 3a: 4). Both nozzles were supplied with air by a centrifugal fan (Lennox Industries) and a custom built manifold, located on the floor below the plane of the table top. With this setup, the jets could be run individually or simultaneously at the desired mean exit velocity.

$$L = 4.4 * d_i * \mathrm{Re}^{1/6} \qquad \textbf{Eq. 3}$$

The PIV imaging system consisted of a 20 W frequency doubled Nd:YLF (λ=527 nm) laser (New Wave Research Pegasus) operated at 1 kHz (Figure 3a,b: 1), and a high-frame-rate CMOS camera (Vision Research Inc. Phantom V9.1), operated at 2 kHz (Figure 3a,b: 5). The seeding consisted of a fine mist of tracer particles produced with a seeding generator (TSI Model 9307) (Figure 3a,b: 7), which was introduced into the flow at the wye connections upstream of each nozzle to allow for homogeneous mixing with the air. The seeding density was independently regulated for each jet by varying the air pressure to the seeding generator inlet with a variable flow regulator.

The laser beam was focused and expanded into a light sheet using a combination of spherical and cylindrical lenses. The laser pulses and camera shutter were synchronized using a pulse generator (BNC model 575) (Figure 3a, b: 6) and the time delay between laser pulses was optimized as 20 μs, based on a maximum pixel shift of eight between consecutive images [3]. Trigger signals for the camera shutter and laser pulses were monitored with an oscilloscope (Tektronix 2024B) (Figure 3b: 8) to ensure proper synchronization.

b. Experimental Matrix

Data were collected under each nozzle in a series of vector field sets corresponding to the camera field-of-view. Each vector field resolved from the PIV images consisted of 60 horizontal and 45 vertical data points (i.e., vectors). The vertical and horizontal spacing between points (i.e., spatial resolution) in any given data set was 0.9 mm. Table 2 lists the distance below each nozzle of the upper and lower edges of the respective vector field sets measured for each flow. In this table, the image levels count downward from the nozzle outlets. Adjacent images were positioned to overlap slightly to provide a continuous set of data, as well as to screen out the spurious data points that commonly occur at the edges. The missing distances at image level eight for the conical jet and image levels eight and nine for the planar jet reflect data sets that were not measured.

The PIV images and corresponding data sets were horizontally positioned beneath each nozzle and aligned with the nozzle centerline. The horizontal distances of the outer edges of data from the nozzle centers are shown in Table 3, with positive values indicating displacement to the right.

Image Level	Conical Jet		Planar Jet	
	Upper Edge (mm)	Lower Edge (mm)	Upper Edge (mm)	Lower Edge (mm)
1	0.5	39.0	3.0	42.0
2	35.5	74.0	37.5	76.5
3	72.0	111.0	74.0	113.0
4	110.0	148.5	107.0	146.0
5	143.0	182.0	143.0	181.5
6	177.0	216.0	179.5	218.0
7	213.0	252.0	215.0	254.0
8	-	-	-	-
9	283.0	322.0	-	-
10	318.0	357.0	317.0	356.0

Table 2: Location and size of field-of-views used in the PIV experiments.

Round Jet		Planar Jet	
Left Edge (mm)	Right Edge (mm)	Left Edge (mm)	Right Edge (mm)
-26.0	25.5	-26.0	26.0

Table 3: Horizontal positioning of PIV images with respect to nozzle center.

c. Data Collection and Processing

Images of the seeded flows (Figure 4a) were processed using dedicated PIV software (LaVision DaVis 7.2) to obtain the two-component velocity fields. A multi pass cross-correlation algorithm with decreasing window size down to 32x32 pixels with 50% overlap was applied. A representative velocity field is shown in Figure 4b.

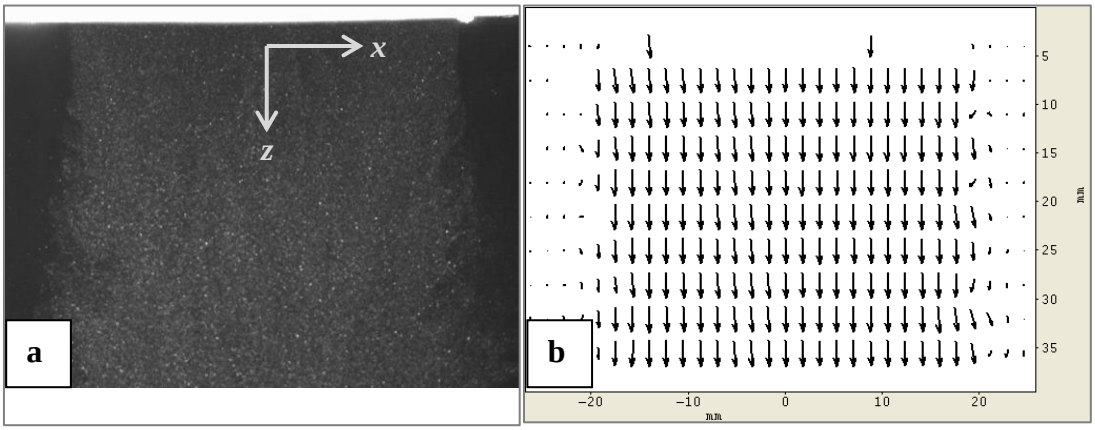

Figure 4: (a) Image showing the seeded jet flow immediately beneath the conical nozzle, indicating the radial (*x*) and vertical (*z*) directions, along with (b) the corresponding velocity field.

Quantities of interest were extracted via algorithms written in-house using MATLAB (R1012a) software. The magnitude of the instantaneous flow velocity (u_i) was calculated at each spatial point (*i)* using the *x* and *z* components of the velocity, according to Eq. 4, where the subscript denotes the spatial location in the two-dimensional (2D) field (see Figure 4). The velocity fluctuations were calculated by subtracting the ensemble average (u_{avg}) (i.e., average of the instantaneous velocity over the 250 PIV vector fields recorded) from the instantaneous velocity (u_i) (Eq. 5). The turbulence intensity was calculated according to Eq. 7, as the ratio of the root-mean-square of the fluctuations (Eq. 6) and the velocity magnitude.

$$u_i = \sqrt{u_x^2 + u_z^2} \qquad \textbf{Eq. 4}$$

$$u_i^{'} = u_i - u_{avg} \qquad \textbf{Eq. 5}$$

$$u_{rms}^{'} = \sqrt{\frac{1}{n}\sum_{i=1}^{n} u_i^{'2}} \qquad \textbf{Eq. 6}$$

$$I = \frac{u_{rms}^{'}}{u_i} \qquad \textbf{Eq. 7}$$

3. Results and Discussion

Experimentally measured centerline velocities for the conical and rectangular nozzles are shown in Figure 5. The velocity magnitude is shown on the vertical axis, normalized by the maximum outlet value (*Uc*). The downstream distance, normalized by the diameter (*D*) or hydraulic diameter (D_H) of the respective nozzle, is displayed on the horizontal axis.

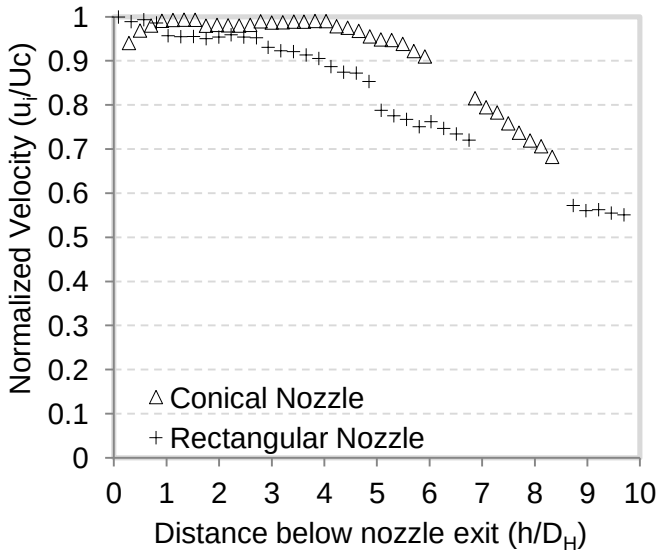

Figure 5: Centerline velocity of jets produced by conical and rectangular nozzles.

The centerline velocity of the jet produced by the conical nozzle does not decrease below 90% of the initial magnitude until approximately six diameters (*D*) downstream. In contrast, the velocity of the planar jet has decayed to 90% of the outlet magnitude by four diameters (D_H) downstream. The breaks in data on both plots represent ranges of data not collected in the experiment.

Figure 6 shows velocity profiles measured across the width of the jet produced by the conical nozzle. These measurements, taken at distances of one, four, and eight nozzle diameters (*h/D*) downstream, illustrate the velocity distribution and state of flow development downstream of the nozzle. The mean velocity is shown on the vertical axis of the plot and is represented as a factor of the maximum outlet velocity (U_C). The position of each measurement along each profile is shown relative to the nozzle centerline as an axial distance (*x*) divided by nozzle diameter (*D*). At one diameter downstream, a nearly "top hat" velocity distribution is clearly visible, indicating a near constant velocity across the width of the jet. At a distance of four diameters downstream, the central portion of the constant velocity zone can still be seen with a magnitude equal to that seen at the outlet, though the velocity of the flow at locations toward the edges of the jet has begun to decrease. At eight diameters, the constant velocity zone is no longer present, and velocity magnitudes across the jet have evolved into a more parabolic distribution.

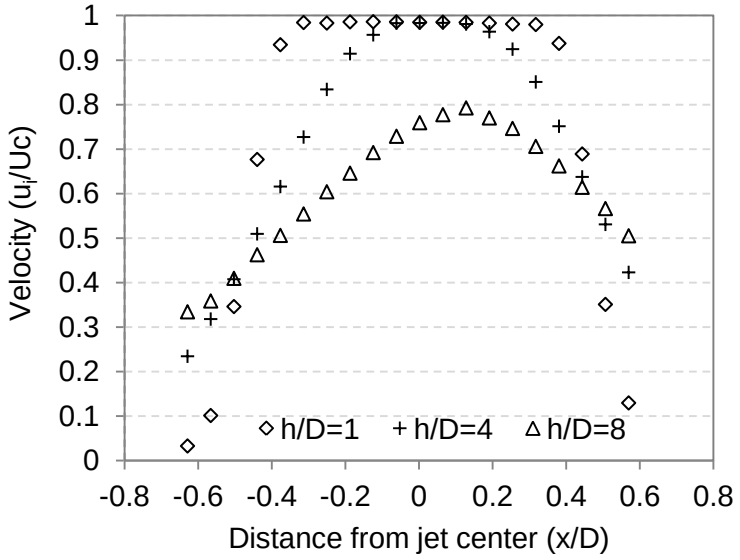

Figure 6: Velocity profiles of jet produced by conical nozzle shown at one, four, and eight diameters downstream of the nozzle exit.

The persistence of constant flow velocities near the centerline of the jet is indicative of the presence of a "potential core" extending beyond a distance of four diameters downstream from the nozzle [4]. Through turbulent interaction with the relatively stationary atmosphere, the mean velocities in this region decrease progressively inward from the jet edge.

The changing shapes of the horizontal (x-direction) velocity profiles shows that the jet was not directed perfectly in the vertical direction. The centerline shift is clearest in the profile positioned eight diameters downstream, where the location of highest velocity has shifted about 0.1 diameters (*x/D = 0.1*) to the right with respect to the center of the outlet. This effect is likely

caused by a defect in the machining of the conical nozzle or to imprecise mounting of the nozzle on the enclosure ceiling.

Figure 7 shows the velocity profiles measured across the jet produced by the rectangular nozzle with the plot scaled in a similar fashion to that of Figure 6. Here the horizontal position of each measurement is normalized by the rectangular nozzle's hydraulic diameter (D_H). Because the rectangular nozzle was wider than the field-of-view of the PIV measurements, the data set does not include jet edges. Here, velocity measurements were sampled at distances of one, four, and nine hydraulic diameters (D_H) downstream. Unlike the near parabolic distributions seen downstream of the conical nozzle exit, velocity magnitudes remain generally unchanged across each of the profiles sampled, with largely flat distributions seen at all three levels. Also in contrast to the jet produced by the conical nozzle, where velocity decay occurred initially at the jet edges and moved progressively inward, mean velocity magnitudes in the planar jet decay across the entire measured width at each vertical (i.e., z) location. This initial decay of mean velocities observed even at the jet centerline indicates the absence of a potential core region and points to turbulent dissipation of velocity in the jet beginning at the nozzle outlet. The edges of each profile show slightly lower velocities, which taper off to the (unresolved) boundary layer at the jet's edges.

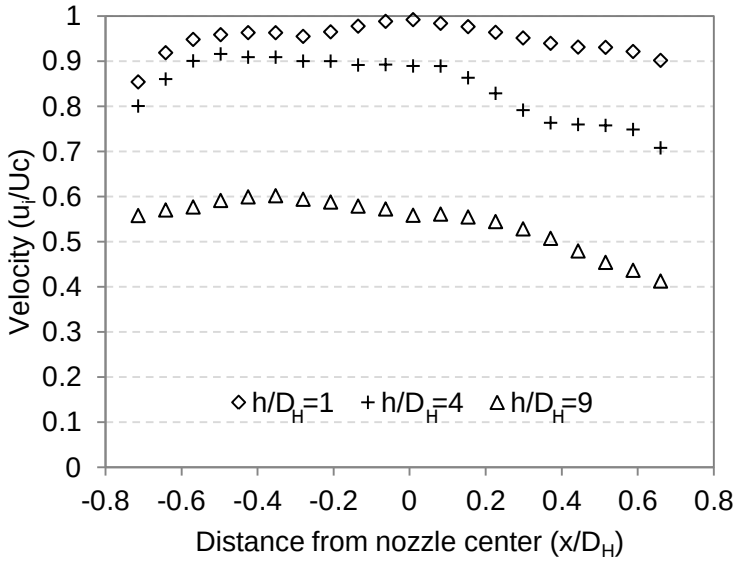

Figure 7: Velocity profiles of the jet produced by the rectangular nozzle shown at one, four, and nine hydraulic diameters downstream of the nozzle exit.

As observed from the conical nozzle velocity profiles, a non-symmetric velocity distribution can be seen along the x-direction for the downstream profiles in Figure 7. The lower velocities on the right side of the jet likely arise from a defect in the planar nozzle itself or its placement.

Turbulence intensity is the degree to which the instantaneous velocity at a point in a flow deviates from its mean value. This deviation is quantified as a percentage of that mean at each point. The turbulence intensity was analyzed for each jet along the same horizontal (x-direction) profiles sampled for the mean velocity, as well as along vertical (z-direction) profiles extending downward from the nozzles.

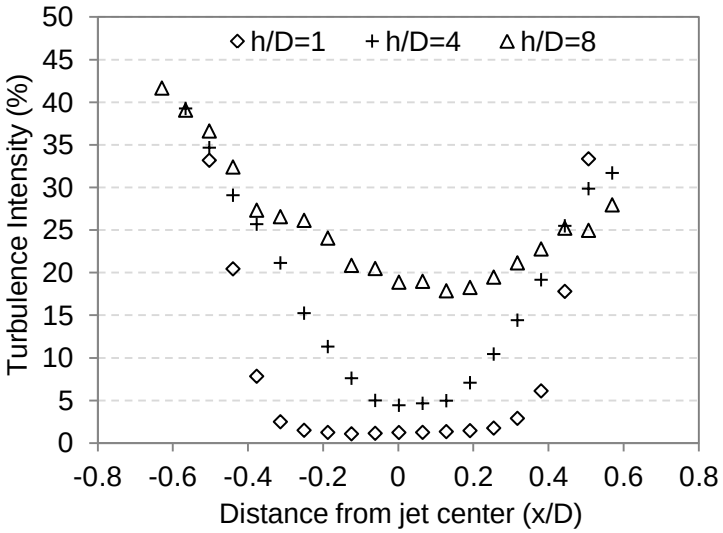

Figure 8: Turbulence intensity profiles of jet produced by the conical nozzle shown at one, four, and eight diameters downstream of the nozzle exit.

Turbulence intensity profiles for the jets produced by the conical and rectangular nozzles are shown in Figures 8 and 9, respectively. Their forms generally follow the inverse of the mean velocity profile plots. For the conical nozzle, the turbulence intensity is minimum nearest the nozzle outlet, inside the potential core where the mean velocity reaches a maximum with minimal deviation. The turbulence intensity increases downstream from the nozzle exit and outward from the centerline toward the edges of the jet, as the uniform velocity of the potential core decays.

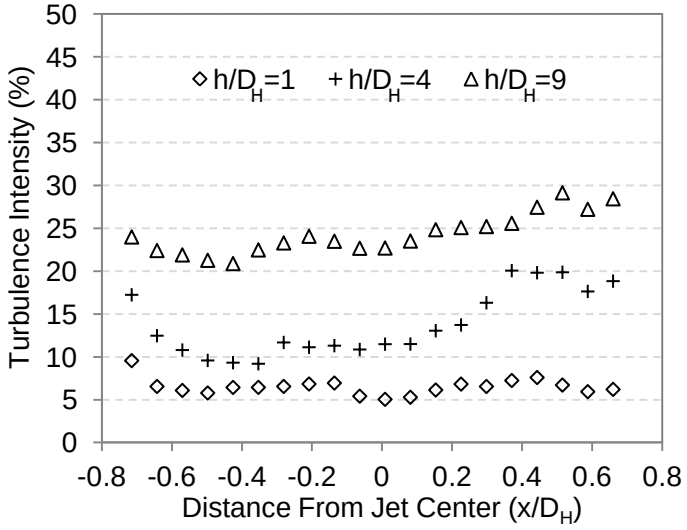

Figure 9: Turbulence intensity profiles of the jet produced by the rectangular nozzle shown at one, four, and nine diameters downstream of the nozzle exit.

In the case of the jet emanating from the rectangular nozzle, the sampled turbulence intensities reflect the generally flat distribution seen in the corresponding velocity profiles. The turbulence intensity at each of these locations increases downstream, as the mean velocity in the flow

progressively decays. The effects of nozzle defects are also clearly seen in the rightward shift of points of minimum turbulence in Figure 8 and the higher downstream turbulence intensity to the right in Figure 9.

Turbulence intensities were also sampled along profiles oriented vertically beneath each nozzle. The values from the conical nozzle jet are shown in Figure 10 with one profile oriented directly underneath the nozzle center and the others offset a distance of 0.4 diameters to either side ($x/D = \pm 0.4$). Downstream distance from the nozzle is quoted along the horizontal axis in terms of the ratio between distance from the nozzle exit (h) and nozzle diameter (D). The plot along the centerline reflects the effects of the potential core identified from the horizontal profiles in Figure 8, where turbulence intensity remains below 5% to around four diameters downstream before progressively increasing as the disintegration of the potential core reaches the jet center. The offset profiles, which experience the initial velocity decay at the edges of the potential core, show turbulence intensities that begin low, but immediately increase and reach levels of 25% to 30%. The generally lower values observed along the right side offset profile ($x/D = +0.4$) reflect the jet's rightward shift downstream of the nozzle exit (see Figure 6).

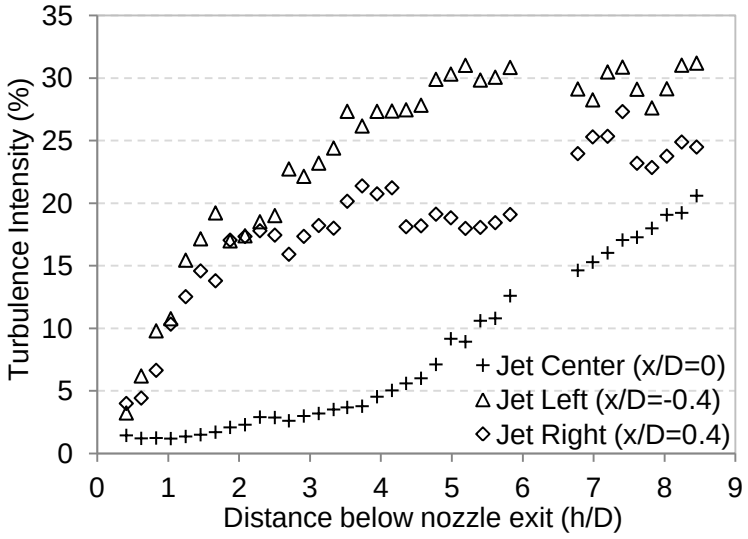

Figure 10: Centerline and offset turbulence intensity profiles for the jet produced by the conical nozzle.

Similarly, turbulence intensity is shown in Figure 11 along corresponding profiles downstream the rectangular nozzle. As before, D_H represents the nozzle's hydraulic diameter (see Eq. 2). As was the case in the horizontal profiles shown in Figure 9, turbulence intensity levels at the center and offset to either side increase in a relatively uniform fashion with increasing distance downstream from the nozzle exit. In the absence of the potential core, the turbulence intensity rises nearly uniformly along the jet cross section, reaching at least 10% at a downstream distance of four diameters ($h/D_H = 4$).

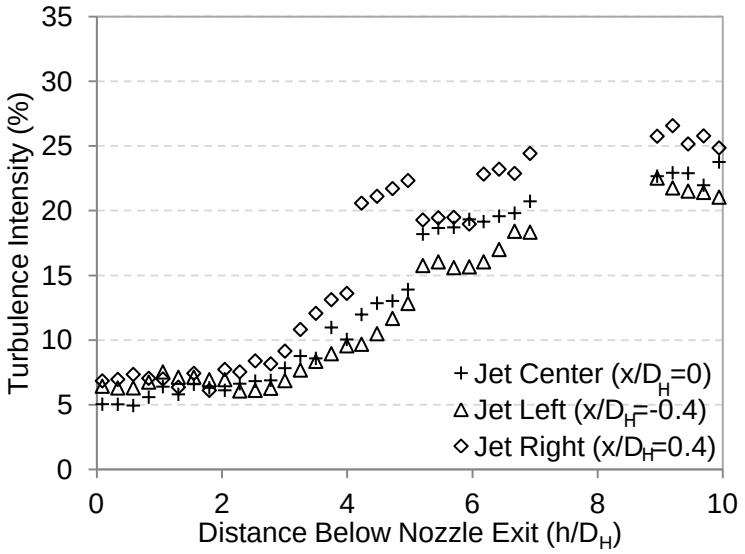

Figure 11: Centerline and offset turbulence intensity profiles for the jet produced by the rectangular nozzle.

4. Impact on Large-Scale Oven Simulation

The accuracy of the predictions made by the large-scale oven simulation is dependent on the faithful representation of the system boundary conditions from the large-scale oven. Turbulence intensity is both one of the most important of these conditions and one of the most difficult to measure. The initial boundary condition assumptions made without information about the degree of turbulence intensity present in the air jet could not be verified as accurate, and thus called into question the predictions of the large-scale oven simulation. The data supplied through this project provides a basis of comparison for establishing the most accurate turbulence modeling method for use in the large-scale simulation and ensuring that simulation predictions more accurately reflect actual conditions. Mean velocity profiles provide a benchmark for predicting the evolution of the jet produced by conical and rectangular nozzles.

5. Impact on Education

Completion of this project allowed both students to fulfill the capstone project requirement necessary for graduation from the Mechanical Engineering program. The overall purpose of the senior design project is to tie together various aspects of the undergraduate curriculum into a project that mimics the type of work done in industry. These basic goals were met, as this project drew upon information learned from such disciplines as Instrumentation, Heat Transfer, and Fluid Dynamics. Also important was the final presentation and the writing of a final report detailing findings and outlining recommendations.

Work on this project, in particular, yielded opportunities to learn unique skills at the undergraduate level. Working with PIV hardware and associated software presented an experience not usually included in undergraduate engineering education and provided familiarity with an advanced measurement technique that has found widespread application in multiple areas of industrial research. Furthermore, this work illustrated the effects of varied nozzle geometry on jet behavior and structure.

The learning opportunities presented stretched beyond the technical. The year-long time scale of the project necessitated longer term planning to stay on track and achieve goals. Key to this effort was an effective division of work between both students to manage the large task load involved. At various points through the duration of the project, progress reports were given to update interested parties on the successes and work remaining.

One of the most important lessons learned was how to design and plan an experiment to achieve the desired goals. Though the essential PIV components were furnished by the university (e.g., laser, optics, camera and processing software) all other aspects of the experimental setup and procedure were designed and developed from scratch. Doing this necessitated the identification at the beginning of the project of the desired outcomes and consideration of the available resources to achieve those tasks. This required a lot of creative thought.

Beyond the educational aspect, this project provided the graduate research effort aimed at improving the function of curing oven air seals with valuable boundary data. The actual turbulence intensities measured will provide a vital baseline for identifying the most accurate turbulence modeling technique. This has far ranging implications for energy savings from industrial curing ovens in the form of reductions in resources use and increased productivity.

6. Conclusions

Use of particle image velocimetry in the senior capstone project provided the students with a unique opportunity to use an advanced measurement technique not often available to those studying at the undergraduate level. The hands-on approach used to create the test setup and procedure provided familiarity with the function and use of PIV that surpassed what could have been gleaned from simply operating a preassembled system. Furthermore, the experimental testing provided practical illustrations of the features and evolution of jets produced by various nozzle geometries.

The project also yielded valuable data in support of the large-scale oven efficiency improvement effort, providing values that would be otherwise very difficult to measure in-situ. Measured mean velocity and turbulence intensity profiles provide both important nozzle outlet boundary conditions as well as a basis of comparison for the validity of the model results. Specifically:

1) The mean velocity in the jet produced by the rectangular nozzle was observed to decay at a progressing rate from the nozzle outlet, with the magnitude decreasing below 90% of the initial outlet level at a downstream distance of four diameters.
2) The mean velocity at the centerline of the jet produced by the conical nozzle remained at maximum outlet levels until four diameters downstream and only dropped to 90% of its initial magnitude after six diameters.
3) Turbulence intensity, in general, followed the inverse behavior of the corresponding velocity profile, increasing as the mean flow velocity decayed. In the jet produced by the conical nozzle, the turbulence intensity reached 1.3% at the nozzle exit, remaining below 5% to a distance of four diameters downstream, and increasing more quickly thereafter.
4) The rectangular jet registered a higher outlet turbulence intensity of 6.3% reflecting its turbulent pipe flow nature. Corresponding to this jet's more evenly distributed velocity

decay, the turbulence intensity rose steadily across the width beyond two diameters downstream and increased above 10% by a downstream distance of four diameters.

Acknowledgments

This material is based upon work supported by the Department of Energy under award number DE-SC0005363 and by a WMU FRACAA grant. The authors are grateful to Mark Lindquist and the staff at Rapid Line, Inc. for making time in their production schedule and allowing access to their curing oven facilities; as well as to Gary Nola, the graduate student heading the oven modeling effort, who consistently made himself available to answer questions. Finally, the authors would like to thank the WMU Office of the Vice President for Research for their recognition and financial support in awarding the 2012 Undergraduate Research Excellence Award.

References

1. Adrian, R. J (2005) "Twenty Years of Particle Image Velocimetry. *Experiments in Fluids*: 39.

2. Munson, B.R., Young, D. F., and T. H. Okiishi (1998). *Fundamentals of Fluid Mechanics*, New York: John Wiley & Sons, Inc, pp. 432.

3. Keane, R. D, and Adrian, R. J. (1990) *Optimization of Particle Image Velocimeters*. Part I. Double Pulsed Systems." Measurement Science and Technology 1.11: 1202-15.

4. Milanovic, I. M, and Hammad, K. J. (2010) *PIV Study of the Near-Field Region of a Turbulent Round Jet*. In ASME 3rd Joint US-European Fluids Engineering Summer Meeting Conference Proceedings, Vol. 1.

List of Symbols

D	-	Nozzle diameter
D_H	-	Nozzle hydraulic diameter
I	-	Turbulence intensity
L	-	Nozzle feed tube length
Re	-	Reynolds number
U_C	-	Maximum nozzle outlet velocity
d_i	-	Nozzle feed tube inner diameter
h	-	Height of the nozzle outlet above the floor
i	-	Spatial location
u_{avg}	-	Velocity ensemble average
u_i	-	Point velocity magnitude
	-	Instantaneous velocity fluctuation
	-	Root mean squared velocity fluctuation
u_x	-	Horizontal component of point velocity
u_z	-	Vertical component of point velocity
x	-	Horizontal direction
z	-	Vertical direction
μ	-	Dynamic viscosity of air
v	-	Kinematic viscosity of air
ρ	-	Air density